Broadband synergy versus oscillatory redundancy in the visual cortex

Louis Roberts[1], Juho Äijälä[1], Florian Burger[1,2], Cem Uran[3,4], Michael A. Jensen[5], Kai J. Miller[5], Robin A.A. Ince[6], Martin Vinck[3,4], Dora Hermes[5,9], Andres Canales-Johnson[1,7,8,9]

[1]*Department of Psychology, University of Cambridge, CB2 3EB Cambridge, United Kingdom*
[2]*The MARCS Institute for Brain, Behaviour, and Development, Western Sydney University, Penrith, NSW, Australia*
[3]*Ernst Strüngmann Institute (ESI) for Neuroscience in Cooperation with Max Planck Society, 60528 Frankfurt am Main, Germany*
[4]*Donders Centre for Neuroscience, Department of Neuroinformatics, Radboud University Nijmegen, 6525 Nijmegen, Netherlands*
[5]*Department of Physiology and Biomedical Engineering, Mayo Clinic, Rochester, MN, USA.*
[6]*Institute of Neuroscience and Psychology, University of Glasgow, Scotland G12 8QB, United Kingdom*
[7]*Neuroscience Center, Helsinki Institute of Life Science, University of Helsinki, P.O. Box 3, Fabianinkatu 33, FI-00014 Helsinki, Finland*
[8]*CINPSI Neurocog, Faculty of Health Sciences, Universidad Católica del Maule, 3460000 Talca, Chile*
[9]*Correspondence to: Andres Canales-Johnson (afc37@cam.ac.uk), Dora Hermes (hermes.dora@mayo.edu))*

Abstract

The cortex generates diverse neural dynamics, ranging from broadband fluctuations to narrowband oscillations in specific frequency bands. Here, we investigated whether broadband and oscillatory dynamics play different roles in the encoding and transmission of synergistic and redundant information. We used information-theoretical measures to dissociate neural signals sharing common information (i.e., redundancy) from signals encoding complementary information (i.e., synergy). We analyzed electrocorticography (ECoG) and local field potentials (LFP) in the visual cortex of human and non-human primates (macaque) to investigate to what extent broadband signals (BB) and narrowband gamma (NBG) oscillations conveyed synergistic or redundant information about images. In both species, the information conveyed by BB signals was highly synergistic within and between visual areas. By contrast, the information carried by NBG was primarily redundant within and between the same visual areas. Finally, the information conveyed by BB signals emerged early after stimulus onset, while NBG sustained information at later time points. These results suggest that broadband activity encodes information synergistically while gamma-band oscillatory activity encodes information redundantly in the visual cortex.

INTRODUCTION

The cortex generates a diverse spectrum of dynamics, ranging from broadband activity to oscillatory activity in specific frequency bands (Bressler and Kelso, 2001; Buzsáki, 2006; Freeman and Skarda, 1985; Hermes et al., 2015a; Miller et al., 2009b; Ray and Maunsell, 2011; Varela et al., 2001; Vinck et al., 2023). A major open question is whether interactions between brain areas are mainly based on broadband dynamics or oscillatory interactions. Several theories have emphasized that coordinated interactions are based on narrowband synchronization or resonance phenomena (Bressler and Kelso, 2001; Fries, 2005; Varela et al., 2001; Vinck et al., 2013). In contrast, other theories emphasize the importance of broadband transients and nonlinear relationships across a broad range of frequencies (Sani et al., 2024; Terada and Toyoizumi, 2024; Vinck et al., 2025, 2023; Yang et al., 2021). Thus, it remains an open question what role these dynamics play in communication and whether they play distinct and complementary roles in encoding and transmitting information (Vinck et al., 2023).

An increasing body of work suggests that information about behavioral and sensory variables can be decoded from many locations, highlighting the distributed nature of neural representations (Allen et al., 2019; Chen et al., 2024; Khilkevich et al., 2024; de Schotten and Forkel, 2022; Shenoy and Kao, 2021; Steinmetz et al., 2019; Stringer et al., 2019; Urai et al., 2022). However, distributed representations do not necessarily encode redundant information; they might also encode synergistic information, concepts derived from information theory. In information theory applied to neural signals (Blume et al., 2024; Combrisson et al., 2024; Daube et al., 2019; Delis et al., 2022; Francis et al., 2022; Gelens et al., 2024; Greco et al., 2024; Ince et al., 2017, 2016; Koçillari et al., 2023; Luppi et al., 2022; Nigam et al., 2019; Olivares et al., 2022; Park et al., 2018; Varley et al., 2023), redundancy measures the shared (or common) information that a set of signals encodes about a stimulus variable. On the other hand, the measure of synergy quantifies the complementary (or extra) information that a set of signals encodes as a whole, above and beyond the information encoded by the sum of the isolated signals. Therefore, redundant and synergistic representations are likely functionally relevant, with redundant representations ensuring robustness but synergistic representations reflecting emergent dynamics in a nonlinear, recurrent coupled system (Gelens et al., 2024). The readout of redundant and synergistic information likely requires dif-

ferent readout mechanisms and network architectures. If their oscillatory or broadband nature governs the integration of distributed signals, then it is plausible that broadband and oscillatory dynamics play different roles in the encoding and transmitting synergistic and redundant information. Previous work has suggested that broadband activity represents auditory prediction errors synergistically in the auditory cortex (Gelens et al., 2024; Greco et al., 2024). However, since the activity in the auditory system is dominated by broadband fluctuations rather than oscillatory dynamics (Canales-Johnson et al., 2021), a direct contrast between broadband vs. oscillatory dynamics is still lacking.

Although narrowband oscillatory activity is not prominent in the auditory cortex, broadband fluctuations and narrowband oscillations are commonly superimposed in other model systems such as the visual system (Hermes et al., 2015a,b, 2017, 2019; Ray and Maunsell, 2011). In fact, several theories have proposed a critical functional role for narrowband gamma oscillations in inter-areal communication and visual coding (Fries, 2005; Fries et al., 2007; Ray and Maunsell, 2015; Salinas and Sejnowski, 2001; Singer, 1999; Vinck and Bosman, 2016; Vinck et al., 2010, 2025, 2013). Therefore, the visual model system is well suited to test whether broadband and narrowband activity subserve the encoding of synergistic or redundant information across nodes. Here, we analyzed electrocorticography (ECoG) and local field potentials (LFP) signals in the visual cortex of human and non-human primates (macaque) and decomposed signals into broadband and narrowband activity. We then investigated to what extent different electrodes (within and between areas) conveyed redundant or synergistic information about visual images via broadband or narrowband gamma oscillations.

RESULTS

To understand how mesoscale field potentials in the visual cortex encode and communicate information about image statistics, we analyzed ECoG data from two human subjects (areas V1, V2, and V3) and LFP data from one macaque (areas V1 and V4) (Figure 1A).

Computing a measure of image homogeneity

We first determined the level of spatial homogeneity of 86 grayscale images previously reported by (Hermes et al., 2019) in human patients and 88 grayscale images previously reported by (Uran et al., 2022) in macaque. For each image, we trained a deep neural network (DNN) (Uran et al., 2022) to predict the spatial pattern in the center of the image by learning its spatial surroundings (Figure 1B; see Methods), and we used the predictability score as an index of image homogeneity. To determine categories of images with high and low levels of spatial homogeneity in the human datasets, we performed a t-test on the predictability scores of two categories of images: gratings, and noise. We observed higher predictability for gratings compared to noise images across images and electrodes in S1 ($t_{(1,110)} = 4.101$, $p < 0.001$) and in S2 ($t_{(1,94)} = 3.08$, $p = 0.002$). As expected, gratings had the highest image homogeneity (S1: $\bar{x} = 0.171$; $\sigma = 0.081$; S2: $\bar{x} = 0.179$; $\sigma = 0.082$) and noise (S1: $\bar{x} = 0.343$; $\sigma = 0.304$; S2: $\bar{x} = 0.307$; $\sigma = 0.274$) patterns had the lowest image homogeneity (Figure 1B). Given the evident predictability of oriented gratings and their usage as low-dimensional visual stimuli, it is no surprise that these stimuli had very high predictability ratings. Conversely, noise images score low on predictability: the contents of one spatial region are not readily predicted by the other. Similarly in M1, we observed higher predictability for gratings ($\bar{x} = 0.244$; $\sigma = 0.146$) compared to natural images ($\bar{x} = 0.009$; $\sigma = 0.013$) across images and electrodes ($t_{(1,470)} = 24.45$ $p < 0.001$).

Decoupling broadband and oscillatory responses from the ECoG and LFP signals

To extract the oscillatory NBG from the non-oscillatory BB neural dynamics in the ECoG signals, we performed the spectral decoupling technique (Miller et al., 2009a; Miller, 2019) (Figure 1D; see Methods). In brief, for each electrode in each subject (S1, S2) and macaque (M1), we computed spectral principal component analysis (SPCA) across the power spectra from all trials. Then, the time series of each trial was reconstructed using the weights of the first and second SPCA, separately (Figure 1D). In each electrodes and datasets (S1: 7 electrodes; S2: 6 electrodes; M1: 126 electrodes: 63 in V1 and 63 in V4; Figure 1A), we observed the characteristic BB first principal component reported in previous ECoG studies during visual and auditory processing (Canales-Johnson et al., 2021; Gelens et al., 2024; Miller, 2019; Miller et al., 2017; Sabra et al., 2019). The BB component spanned frequencies from 1 to 200 Hz without a characteristic peak (Figure 2A, in dark green).

In contrast, the second principal component peaked in the frequency range of the oscillatory, narrowband gamma band (NBG: ~30-80 Hz), and it was observed in 5 out of 7 electrodes of S1, in 6 out of 6 electrodes of S2, and in 58 out of 63 electrodes in M1 (Figure 2A, in light green). While the BB response is induced by all images, including spatially heterogeneous images (Hermes et al., 2015a, 2019), the NBG response is predominantly induced by spatially homogeneous images such as gratings (Hermes et al., 2015a, 2019). Note that these induced BB and NBG changes are best appreciated after ~100 ms when transient evoked responses have less influence on the signal. A representative electrode (area V1) for S1, S2, and M1 is depicted in Figure 2B for gratings (in purple), noise, and natural images (in yellow), reconstructed with the BB (dark green) and NBG components (light green).

Information about image homogeneity is encoded in BB and NBG signals

After decoupling the non-oscillatory BB and the oscillatory NBG responses from the ECoG and LFP signals, we quantified the amount of information encoded in the signals about image homogeneity using information-theoretic measures. To this end, we computed Mutual Information (MI) between trials corresponding to images with high and low spatial homogeneity (Figure 2C) using the Gaussian-Copula Mutual Information

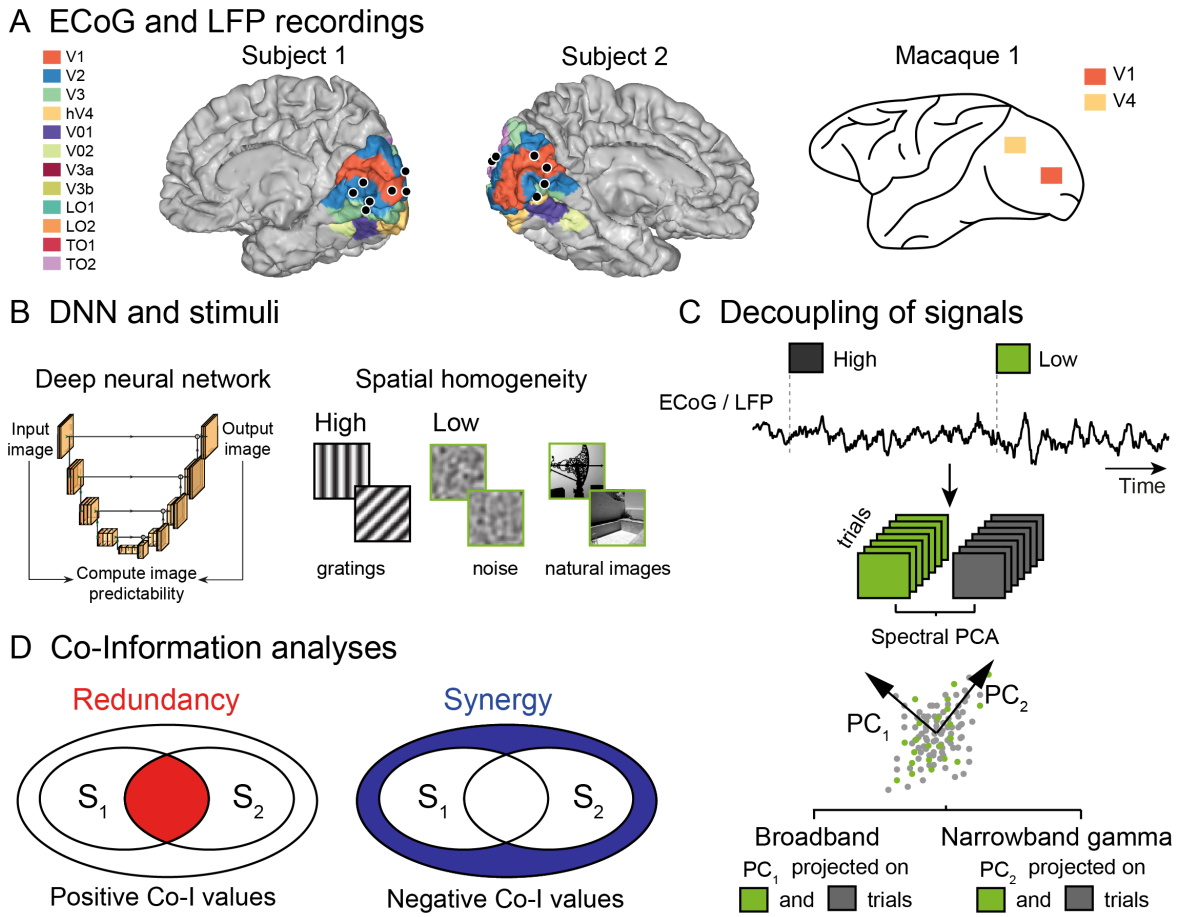

Figure 1: Redundancy and synergy analyses, stimuli, and decoupling neural ECoG and LFP responses. **(A)** Location of the electrodes implanted in Subject 1 (S1) and Subject 2 (S2) (black dots) rendered on estimates of early visual areas, and schematic representation of Macaque 1 (M1) brain with electrode locations (orange and yellow squares). **(B)** The spatial predictability of images was quantified using a technique based on self-supervised, deep neural networks (DNN; see Methods). In brief, a DNN is trained to predict visual images into the receptive fields (RFs). A mask of approximately the same size as the recording site's RF is applied to an image. The image with the mask is then entered as an input to a DNN with a U-net architecture. This DNN predicts the full image, i.e., the image content behind the mask is filled in. Stimulus predictability is computed by comparing the ground-truth input image and the predicted image and then using it for network optimization during the training stage. The images were identical to those used in a prior ECoG study and grouped into several stimulus categories (S1 and S2: space, orientation, contrast, sparsity, and coherence; M1: orientation, and natural images). The images with the highest predictability score (high spatial homogeneity: gratings) were compared against those with the lowest predictability scores (low spatial homogeneity: noise and natural images). **(C)** Decoupling neural signals from ECoG and LFP data. Epochs corresponding to high homogeneity (black) and low homogeneity (green) images are used to compute the broadband (BB) response and narrowband gamma (NBG) response. BB signals are computed by reconstructing the time series of each stimulus category trial with the first spectral principal component (SPCA) of the ECoG/LFP signal; NBG are computed by reconstructing the same time series with the second principal component (SPCA) of the ECoG/LFP signal (see Methods). **(D)** Schematic representation of redundancy and synergy analyses computed using co-information. Each inner oval (S1 and S2) represents the mutual information between the corresponding ECoG/LFP signals and the stimuli category. The overlap between S1 and S2 represents the redundant information about the stimuli (red; left panel). The outer circle around S1 and S2 represents the synergistic information about the stimuli (blue; right panel). S1 and S2 can be signals from the same area (e.g. V1) or between areas (e.g. V1 and V2).

(GCMI) estimator (Ince et al., 2017). Within the framework of information theory, MI is a statistical measure that quantifies the strength of the dependence (linear or nonlinear) between two random variables. It can also be seen as the effect size, quantified in bits, for a statistical test of independence. Thus, we used MI separately for the BB and NBG responses to quantify the difference between image categories on a common effect size scale. We observed significant information encoded in the BB (dark green) and NBG (light green) signals after contrasting gratings versus noise in S1 and S2, and gratings versus natural images in M1 (Figure 2C).

Although both BB and NBG responses encoded significant information about the spatial homogeneity of images, we did observe some differences between the two types of dynamics (Figure 2B). In particular, the significant MI effects in the BB signals manifested at earlier latencies than the NBG effects, and they were more transient (or less sustained) than the NBG effects. This was observed in S1 (BB: ~40-150 ms; NBG: ~80-350 ms after stimuli presentation), S2 (BB: ~70-220 ms; NBG: ~100-300 ms after stimuli presentation), and M1 (BB: ~50-100 ms; NBG: ~60-350 ms after stimuli presentation).

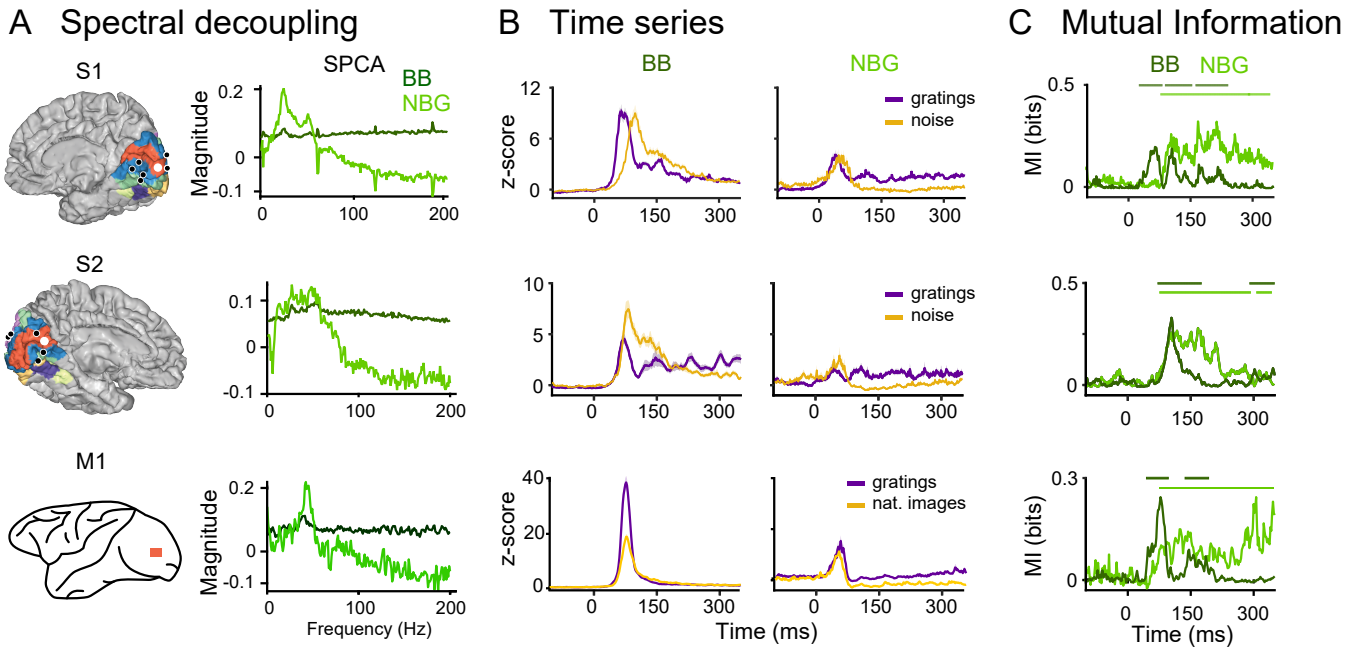

Figure 2: Spectral decoupling and mutual information analyses. **(A)** Spectral decoupling from a V1 electrode in Subject 1 (S1) and Subject 2 (S2) (in white), and from a V1 electrode in Macaque 1 (M1) (in orange). The magnitude of the first (dark green) and second (light green) spectral principal component (SPCA) is shown between 1 and 200 Hz. The first SPCA is the non-oscillatory, broadband (BB) component and the second SPCA is the oscillatory, narrow-band gamma (NBG) component. **(B)** Time-series average across gratings (purple), and noise (yellow) trials, reconstructed with the BB (left panel) and NBG components (right panel) for S1, S2, and M1. **(C)** Mutual information analyses between gratings (dark green) and noise images (light green) for S1 and S2, and between gratings and natural images for M1. Mutual information (in bits) quantifies the effect size of the difference between the corresponding image categories, representing the amount of information encoded in the signals about the stimuli difference. The significant time points after a permutation test are shown as bars over the MI plots.

Temporal redundancy in BB and NBG signals

The finding that BB and NBG signals encode information about image homogeneity raises the question of whether the information encoded within visual regions is shared (redundant) or complementary (synergistic) across time. To answer this question, we separately computed synergistic and redundant information across time using co-information (co-I) for the BB and NBG responses. Co-I analyses revealed temporal clusters of synergistic information (in blue) and redundant information (in red) across time within BB and NBG signals in S1 and S2 when contrasting gratings versus noise images (Figure 3).

Regarding the dynamics of redundant information within BB and NBG signals, we observed different patterns of temporal redundancy for the two signals. Redundancy quantifies the degree to which two time points carry the same trial-by-trial information about the stimulus contrast. This is conceptually similar to the temporal generalisation method (King and Dehaene, 2014), which quantifies the similarity of a multivariate predictive response pattern over time. Similarly, different temporal patterns of redundancy can reveal different signatures of information representation. A diagonal pattern indicates what King and Dehaene (2014) term a *chain*, where a sequence of discrete generators represent the stimulus over time. In contrast, a square pattern indicates a *sustained* response, which is more likely to result from a single process maintained over time.

In the case of redundancy, a diagonal pattern indicates a continually evolving representation of information, a representation that is distributed over time. In such a system, a downstream readout would benefit from integrating the signal over time, as later time points continue to provide new information. In the BB signals, diagonal redundancy was observed in S1 and S2 (Figure 3A,C) and M1 (Figure 5A).

Instead, a sustained block pattern was observed in the NBG signals. Redundancy over a large temporal region suggests a unitary information processing event in which the same information is obtained whichever time point you sample from. In this case, a downstream processor would only need to observe one time point to get all the information, although integration might still have benefited from an SNR perspective. In the NBG signals, we observed sustained redundancy over time across the entire period after stimuli presentation in S1 and S2 (Figure 3B, D; and M1 (Figure 5B).

To directly compare potential differences in how BB and NBG signals encode redundant representations about image homogeneity, we quantified and statistically contrasted the temporal extension of redundancy between BB and NBG signals (see Methods). We observed more temporal redundancy in NBG compared to BB signals in S1 ($t_{(1,9)} = 2.83$; $p = 0.019$; Figure 3C); and S2 ($t_{(1,12)} = 3.90$; $p = 0.003$; Figure 3F); and M1: ($t_{(1,62)} = 8.30$; $p < 0.001$; Figure 5C), and also more generally in co-I (S1: $t_{(1,9)} = 2.30$; $p = 0.046$; S2: $t_{(1,12)} = 3.28$; $p = 0.009$; M1: $t_{(1,62)} = 7.70$; $p < 0.001$).

Temporal synergy in BB and NBG signals

In contrast to redundancy, temporal synergy within BB signals was observed off-diagonally between early and late time

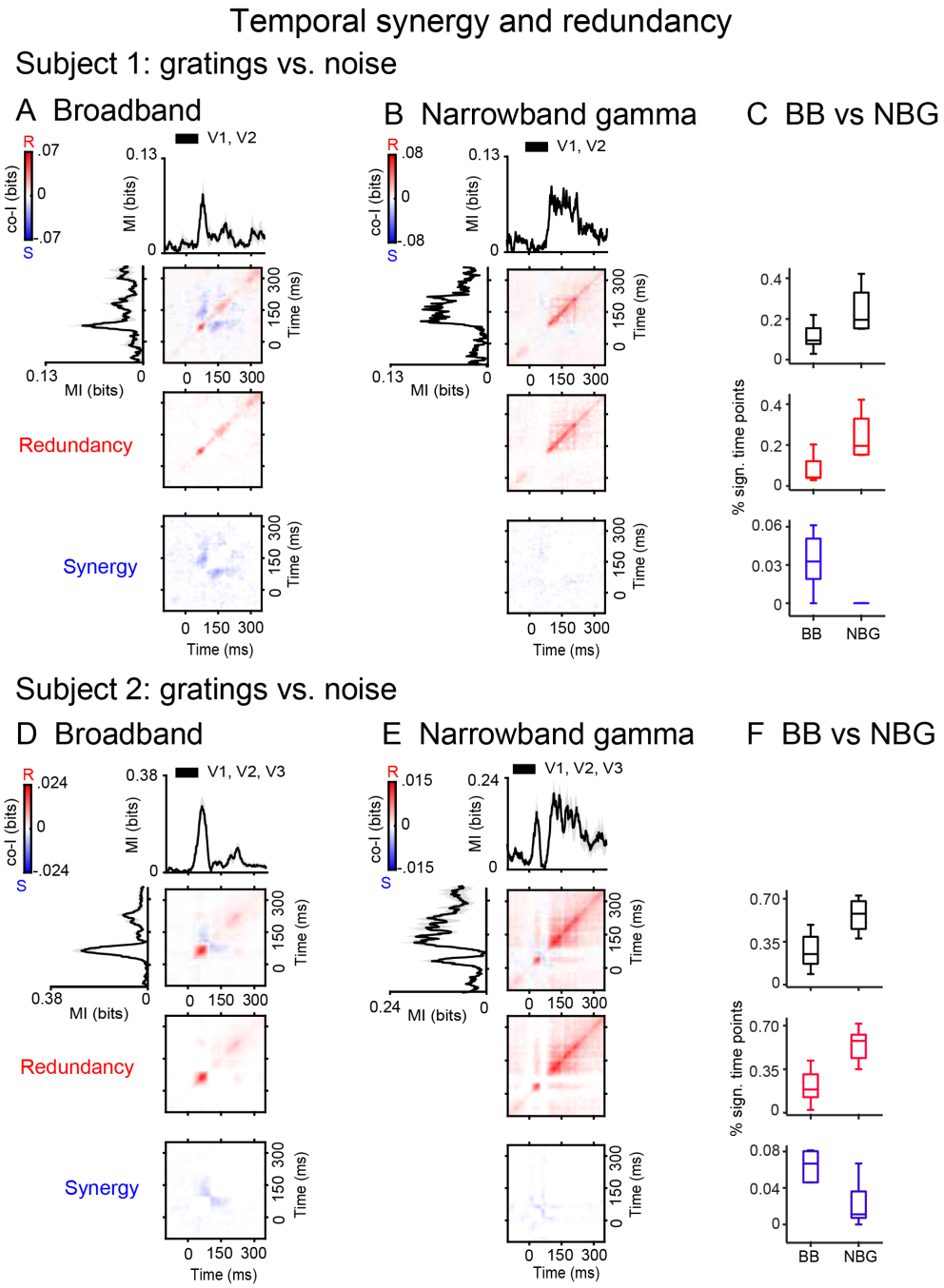

Figure 3: Temporal synergy and redundancy within visual areas in the human brain. Co-information revealed synergistic and redundant temporal patterns within the visual cortex in Subject 1 and Subject 2. (**A, D**) Co-information charts for BB signals. (**B, E**) Co-information charts for NBG signals. Black traces represent the MI between gratings and noise trials for the corresponding signals. Error bars represent the standard error of the mean (S.E.M) in V1 and V2 electrodes for S1 (**A, B**), and in V1, V2 and V3 electrodes for S2 (**D, E**). Temporal co-I was computed within visual areas across time points between -100 to 350 ms after image presentation. The average across individual recording sites is shown for the complete co-I chart (red and blue panel); for positive co-I values (redundancy only; red panel); and negative co-I values (synergy only; blue panel). (**C, F**) Box plots display the sample median alongside the interquartile range. Samples represent the percentage of significant time points observed in each electrode for co-I (black boxes), redundant (positive values; red boxes), and synergistic information (negative values; blue boxes) in the corresponding BB and NBG signals.

points in S1 and S2 (Figure 3A,C), and M1 (Figure 5B). This off-diagonal synergy has a characteristic pattern with two lobes originating from a common starting point aligned with each temporal axis (Gelens et al., 2024). As for redundancy, we can ask what system would lead to this profile. One possibility is that the neural system undergoes a discrete change of state at the time point corresponding to the origin of the two synergy nodes. This means that the signal obtained from any time point

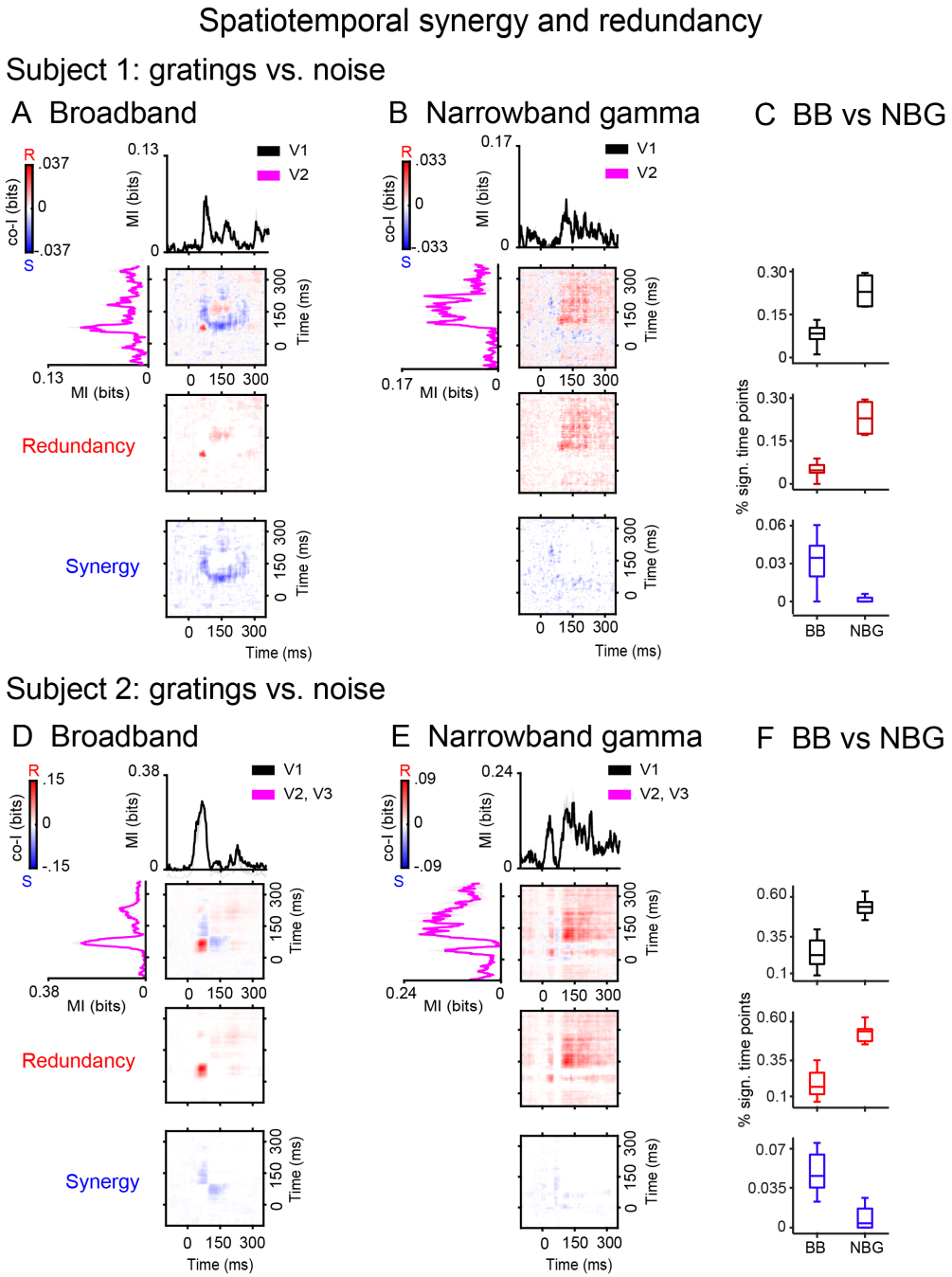

Figure 4: Spatiotemporal synergy and redundancy between visual areas in the human brain. Co-information revealed synergistic and redundant temporal patterns between visual areas in Subject 1 and Subject 2. (**A, D**) Co-information charts for BB signals. (**B, E**) Co-information charts for NBG signals. Black traces (electrodes in V1) and magenta traces (electrodes in V2, and V3) represent the MI between gratings and noise trials. Error bars represent the standard error of the mean (S.E.M) between the corresponding electrodes. Co-I was computed between each pair of electrodes (V1-V2 for S1; V1-V2 and V1-V3 for S2) and across time points between -100 to 350 ms after image presentation. The average across inter-areal electrode pairs is shown for the complete co-I chart (red and blue panel); for the positive co-I values (redundancy only; red panel); and the negative co-I values (synergy only; blue panel). (**C, F**) Box plots display the sample median alongside the interquartile range. Samples represent the percentage of significant time points observed in each electrode for co-I (black boxes), redundant (positive values; red boxes), and synergistic information (negative values; blue boxes) in the corresponding BB and NBG signals.

after the origin of the synergy nodes gives information about the state of the neural system, which improves the readout of the represented stimulus information. This is how synergy can arise between time points even when one does not carry any stimulus information directly (i.e., without significant MI at those time points).

To compare these synergistic patterns to the redundant ones, we quantified and statistically contrasted the temporal exten-

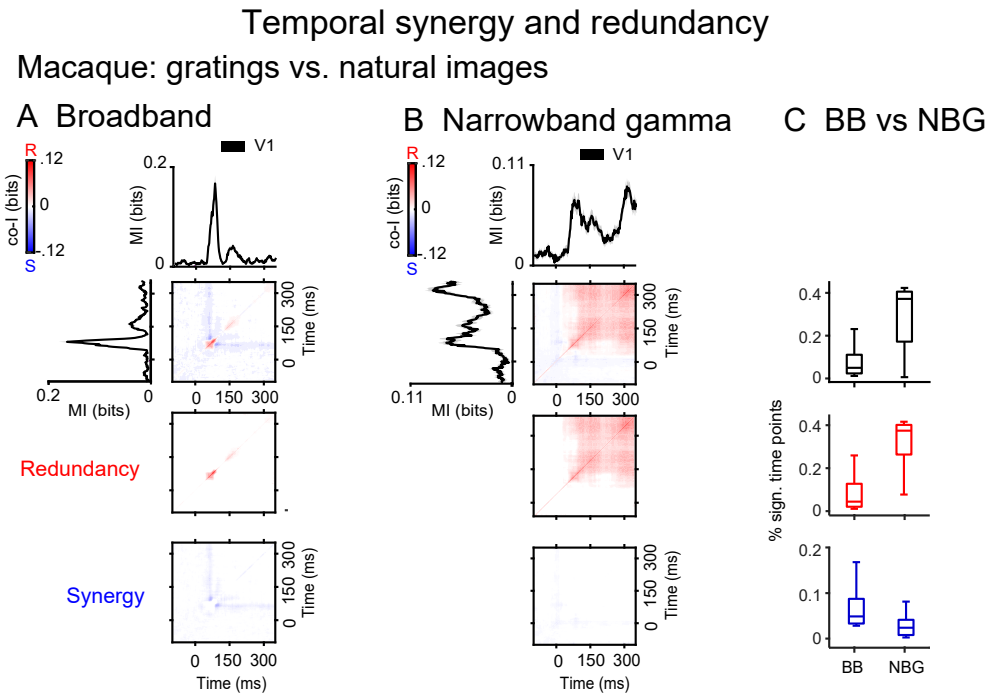

Figure 5: Temporal synergy and redundancy within visual areas in the macaque brain. Co-information revealed synergistic and redundant temporal patterns within the visual cortex in Macaque 1. (**A**) Co-information charts for BB signals in V1. Co-information charts for NBG signals in V1 (**B**). Black traces (V1) represent the MI between gratings and natural images for the corresponding signals. Error bars represent the standard error of the mean (S.E.M) across the corresponding signals. Temporal co-I was computed within visual areas across time points between -100 to 350 ms after image presentation. The average across individual recording sites is shown for the complete co-I chart (red and blue panel); for positive co-I values (redundancy only; red panel); and negative co-I values (synergy only; blue panel). (**C**) Box plots display the sample median alongside the interquartile range. Samples represent the percentage of significant time points observed in each electrode for co-I (black boxes), redundant (positive values; red boxes), and synergistic information (negative values; blue boxes) in the corresponding BB and NBG signals.

sion of synergy between BB and NBG signals (see Methods). Interestingly, and in contrast to temporal redundancy, we observed more temporal synergy in BB compared to NBG signals in S1 ($t_{(1,9)} = 3.06$, $p = 0.017$; Figure 3C); and S2 ($t_{(1,12)} = 3.27$, $p = 0.012$; Figure 3F), and M1 ($t_{(1,62)} = 2.42$, $p = 0.016$; Figure 5C).

Spatiotemporal redundancy in BB and NBG signals

The observation that BB and NBG signals convey distinct types of information about image homogeneity within visual regions raises the question of whether BB signals and NBG signals would primarily encode synergistic and redundant information *between* visual areas, respectively.

Regarding redundancy, we observed different spatiotemporal patterns between areas in the BB and NBG signals. Similarly to the results observed within areas, interareal interactions in the NBG signals were highly sustained over time compared to the redundant patterns observed between BB signals, which exhibited redundancy along the diagonal (Figure 4). In S1, redundant interactions were observed between areas V1-V2 (Figure 4A,B); and between areas V1-V2/V3 in S2 (Figure 4C,D), and between V1 and V4 in the case of M1 (Figure 6).

We quantified and statistically contrasted differences between BB and NBG signals as described above, this time between the corresponding visual areas. Again, we observed higher temporal redundancy in NBG compared to BB signals in S1 ($t_{(1,9)} = 3.90$; $p = 0.003$; Figure 4C); and S2 ($t_{(1,12)} = 7.39$; $p < 0.001$; Figure 4F), and also in co-I (S1: $t_{(1,9)} = 6.46$; $p < 0.001$; S2: $t_{(1,12)} = 6.10$; $p < 0.001$).

In the case of M1, since we did not observe NBG signals in V4, we only report V1-V4 interactions in the BB signals (Figure 6). To quantify whether the spatiotemporal redundancy and co-I were statistically significant above chance, we performed permutation tests for co-I and redundancy charts separately (see Methods). Significant redundancy between V1 and V4 was observed in 3597 out of 3969 electrode pairs (90.6%). Similarly, we observed significant co-I in 3686 out of 3969 V1-V4 electrode pairs (92.8%).

Spatiotemporal synergy in BB and NBG signals

In contrast, and consistent with the findings within regions, interareal synergistic information was mainly observed in the BB signals in S1 and S2 (Figure 4A,C) and in M1 (Figure 6). Across species, interareal synergy was observed off-diagonally between the peak of the MI signal in one region and later time points of the MI signals in another region (S1: Figure 4A,C; S2: Figure 4A,C; M1: Figure 6). As per redundancy, we contrasted the spatiotemporal synergy between BB and NBG signals between the corresponding visual areas. We observed higher spatiotemporal synergy in BB compared to NBG signals in S1 ($t_{(1,9)} = 3.42$; $p = 0.004$; Figure 4C); and S2 ($t_{(1,12)} = 4.72$; $p < 0.001$; Figure 4F). In the case of M1, to quantify whether spa-

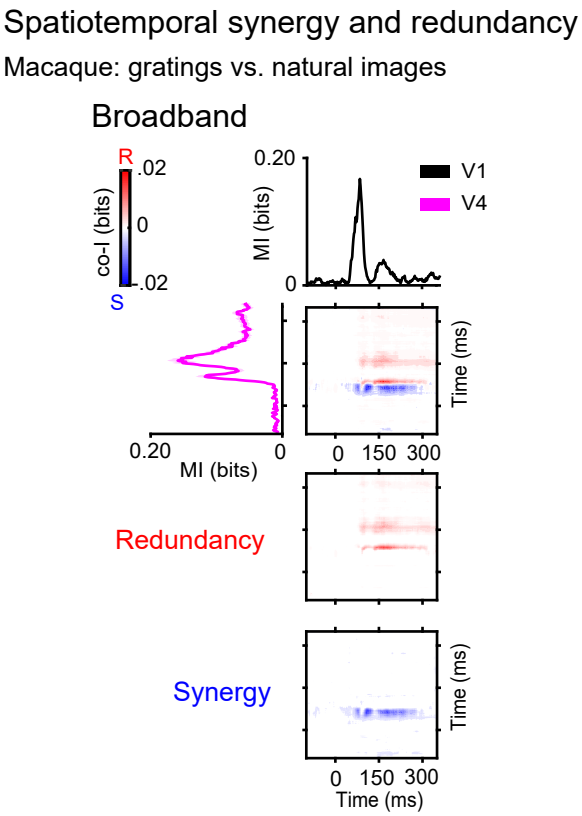

Figure 6: Spatiotemporal synergy and redundancy between visual areas in the macaque brain. Co-information revealed synergistic and redundant spatiotemporal patterns between BB signals across recording sites. Black traces (electrodes in V1) and magenta traces (electrodes in V4) represent the MI between gratings and noise trials. Error bars represent the standard error of the mean (S.E.M) between the corresponding electrodes. Co-I was computed between each pair of electrodes (V1-V4) and across time points between -100 to 350 ms after image presentation. The average across inter-areal electrode pairs is shown for the complete co-I chart (red and blue panel); for the positive co-I values (redundancy only; red panel); and the negative co-I values (synergy only; blue panel).

tiotemporal synergy between V1 and V4 was significant above chance, we performed permutation tests in the synergy charts (Figure 6). Significant spatiotemporal synergy between V1 and V4 was observed in 1721 out of 3969 electrode pairs (43.4%).

DISCUSSION

In the visual system, broadband fluctuations and narrowband gamma oscillations are commonly superimposed (Hermes et al., 2015a, 2019; Miller et al., 2009a; Ray and Maunsell, 2011). It remains an open question what role these dynamics play in communication and whether they play distinct and complementary roles in encoding and transmitting information (Vinck et al., 2025, 2023). We investigated whether broadband and oscillatory dynamics play different roles in encoding and transmitting synergistic and redundant information. The redundancy metric captures the shared (or common) information that a set of signals encodes about a stimulus variable. On the other hand, the metric of synergy quantifies the complementary (or extra) information that a set of signals encodes as a whole, above and beyond the information encoded by the sum of the isolated signals (Gelens et al., 2024; Ince et al., 2017).

To test this hypothesis, we recorded from multiple visual areas in the macaque and human cortex and decomposed signals into broadband and narrowband gamma activity. Broadband signals already carried substantial information about visual images at short latencies after stimulus onset, while narrowband activity carried information in a sustained manner, consistent with previous hypotheses (Vinck et al., 2023). We show broadband signals encoded significant synergistic information about visual images, whereas narrowband signals were predominantly redundant.

Redundant versus synergistic interactions

Empirical studies in several species and sensory modalities have shown that synergy and redundancy have functional relevance for encoding stimuli and task variables (Blume et al., 2024; Combrisson et al., 2024; Delis et al., 2022; Francis et al., 2022; Gelens et al., 2024; Greco et al., 2024; Koçillari et al., 2023; Nigam et al., 2019; Olivares et al., 2022; Park et al., 2018; Varley et al., 2023). In the auditory system, broadband signals between the primary auditory cortex (A1) and frontal areas exhibit synergistic encoding of prediction errors (Gelens et al., 2024). Computational modeling suggests that such synergistic relations between distributed prediction error signals can result from nonlinear recurrent dynamics between regions (Gelens et al., 2024). In the visual system, laminar recordings in the primary visual cortex (V1) indicate that synergistic interactions

can decode visual stimuli more effectively than redundant interactions, even when faced with noise and overlapping receptive fields (Nigam et al., 2019). In contrast, LFP recordings across the olfactory system show that narrowband oscillations exhibit higher levels of redundant information about odorant stimuli (Olivares et al., 2022). In human MEG recordings, theta oscillations (3-7 Hz) in the temporal cortex represent auditory and visual input redundantly during the multimodal integration of audio-visual speech signals (Park et al., 2018). Contrarily, the same narrowband oscillations in the motor and inferior temporal cortex represent the inputs synergistically (Park et al., 2018).

What mechanisms account for the differences in synergy and redundancy observed here? We posit that synergy results from nonlinear recurrent interactions between nodes, such that information resides in the joint pattern of activity across nodes. In support of this idea, a recent study shows that adding recurrent interactions between nodes causes a switch from redundant to synergistic representations (Gelens et al., 2024).

By contrast, redundancy in narrowband oscillatory signals may simply reflect that linear transformations yield communication at the same frequency, and only relay information. Thus, linear information transmission leads to redundancy and signal transfer within the same frequency band. We have previously shown that a sending and receiving neural population will naturally exhibit coherent activity because spiking activity in a sending area causes synaptic potentials in the same area and highly correlated synaptic potentials in another receiving area (at a delay) (Dowdall et al., 2023; Dowdall and Vinck, 2023; Schneider et al., 2021). Hence, coherence can be a consequence of linear signal transmission rather than the cause of inter-areal communication. Furthermore, we showed that narrowband gamma-band signals may not impact spiking activity in downstream areas, such that they primarily contribute to inter-areal coherence via the generation of subthreshold synaptic potentials in downstream neurons (Schneider et al., 2023; Spyropoulos et al., 2022b). Finally, gamma oscillations in the visual cortex are well approximated by linear models (damped harmonic oscillators) (Spyropoulos et al., 2022a), such that integration within the gamma-frequency band may take place via linear resonance rather than nonlinear entrainment mechanisms (Lewis et al., 2021). Thus, the redundancy between narrowband signals shown here may reflect linear transmission between sites. Even if there are nonlinear interactions within the same frequency band, communication within the same frequency band may typically involve relaying information, leading to redundancy rather than extracting patterns via nonlinear transformations. In fact, modeling studies investigating selective communication via coherence (Communication-through-Coherence; CTC) have focused on scenarios where information is relayed between areas (Akam and Kullmann, 2012).

Functional implications

Our findings suggest that broadband and narrowband dynamics have complementary functions in the encoding and transmission of information. We posit that the characteristics of broadband activity may be ideally suited for transmitting synergistically encoded information. Notably, synergistic information represented by two populations X and Y typically requires nonlinear read-out mechanisms in a receiving area Z. For example, in the case of the classic example of a synergistic function, the XOR-gate (Down and Mediano, 2025; Timme et al., 2014), a receiver should compute a function $g(X, Y)$ to extract the information encoded in the joint activity pattern rather than an additive function $f(X) + h(Y)$. In other words, a synergistic code in X and Y might imply that X and Y exert non-separable, nonlinear influences. Nonlinear integration mechanisms in the cortex may predominantly rely on broadband signals that allow for interactions across frequencies (Vinck et al., 2023), which agrees with our finding that broadband activity predominantly carries synergistic information. Notably, this broadband activity carried information especially early after stimulus onset, while oscillatory activity carried information substantially later. This finding agrees with the hypothesis that perceptual inference is mainly subserved by transient broadband activity rather than sustained narrowband activity (Vinck et al., 2025). Such a rapid inference may depend on nonlinear recurrent interactions between areas converging to a joint multi-areal attractor state, where information is synergistically encoded.

Visual processing is a highly nonlinear process (Cohen et al., 2020; DiCarlo et al., 2012) that depends partially on recurrent interactions (Kar et al., 2019). In fact, clusters of pixels collectively provide synergistic information about an object's identity. This is because individual pixel values alone offer very little insight into what the object is. However, when these pixel values are considered together, the relational information in the pattern improves object recognition. Therefore, a system that performs perceptual inference by nonlinearly integrating information over space can be expected to exhibit synergistic representations. This principle can even be seen when nodes are explicitly initialized in an oscillatory manner: A recent modeling study has shown that a recurrent neural network that is initialized with oscillating nodes gradually desynchronizes and increases its heterogeneity across nodes during the learning of a pattern recognition task, indicating that cross-frequency relations are required for performing a complex pattern recognition task (Effenberger et al., 2025).

Interestingly, early theories on perceptual integration emphasized that perceptual binding relies on synchronized oscillatory firing (Singer, 1999). In such a case, the information about the object (i.e., representing the same object) would be shared across nodes, leading to redundant representations. An alternative possibility is that perceptual binding relies on synergistic representations that emerge from nonlinear interactions between nodes. Indeed, previous work suggests that nonlinear interactions across distributed nodes rather than linear interactions or spectral power distinguish different perceptual states, given a constant sensory input (Canales-Johnson et al., 2023, 2020). Here, an interesting connection can be made with theories of consciousness emphasizing that consciousness reflects integrated information (Tononi et al., 2016), as synergistic representations among nodes (e.g. X and Y) imply intrinsic causal influences that are nonseparable to extract the information.

Compared to broadband information, which was particularly strong at earlier phases and became weak during late stimulus

phases, information at later stimulus phases was carried predominantly by narrowband gamma activity, with information represented redundantly. This may suggest that information is sustained with a higher degree of redundancy across space and time after the initial stimulus phase in which information is synergistically encoded via broadband activity. Indeed, narrowband oscillatory activity may be functionally well suited to sustain representations over time in an efficient and stable manner (Chalk et al., 2016; Vinck et al., 2025). Notably, the emergence of narrowband gamma activity may be restricted to a subset of visual stimuli, while broadband activity may be ubiquitous across stimuli. In particular, narrowband gamma activity emerges predominantly, or exclusively, for a subset of natural stimuli (Hermes et al., 2015a,b, 2019; Peter et al., 2019; Uran et al., 2022). Moreover, gamma is generally strongest for visual stimuli that are low-dimensional and have a high degree of homogeneity/predictability in visual inputs across space and time (Hermes et al., 2019; Peter et al., 2019; Shirhatti et al., 2022; Uran et al., 2022; Vinck and Bosman, 2016). Hence, narrowband gamma may emerge mainly for stimuli with a high degree of redundant information across space, which fits the present finding that narrowband gamma carries redundant information representations.

To sum up, the present work shows a new principle: synergistic information in broadband activity and redundant information in gamma-band oscillations. This highlights a potential dual role for these two features of cortical dynamics in sensory processing, with broadband dynamics subserving nonlinear pattern recognition and oscillations subserving information sharing, contributing to robustness.

Authorship contributions

Conceptualization: AC-J and DH. Data analysis: LR, FB, JÄ, and AC-J. Human recordings: DH, KJM, MAJ. Macaque data: CU, MV. Software and methods for human and macaque data: AC-J, CU, MV, RI, and DH. Visualization: LR, FB, JÄ, and AC-J. Writing and editing: AC-J, LR, MAJ, JÄ, MV, RI and DH. Supervision: AC-J.

Acknowledgments

ACJ is funded by an ANID/FONDECYT Regular (1240899) and ANID/FONDECYT Regular (1251273) research grants. DH is funded by the National Eye Institute of the National Institutes of Health under Award Number R01EY035533 and R01EY023384. The content is solely the responsibility of the authors and does not necessarily represent the official views of the National Institutes of Health. This project was funded by the Neurological Foundation of New Zealand Grant (1839RF, to Corinne Bareham) and the Royal Society of New Zealand Marsden (MAU2011, to Dr. Corinne Bareham). MV and CU were financed by an ERC starting grant (850861) SPATEMP, DFG VI Grants (908/5-1 and 908/7-1), an NWO VIDI Grant, and the Dutch Brain Interface Initiative (DBI2).

Competing interests Statement

The authors declare no competing interests.

METHODS

Data acquisition

The data analyzed in this study consisted of ECoG recordings in two human subjects and one macaque monkey. The data acquisition details are reported in full in Hermes et al. (2019), and data is available here: https://osf.io/q4yad.

This study modelled the broadband and gamma responses in early visual areas to 86 different stimuli varying across spatial location, orientation, contrast, sparsity, and coherence dimensions. ECoG potentials were recorded at 1528 Hz in the left hemisphere of S1 and the right hemisphere of S2 using 128-channel Tucker Davis Technologies and Micromed Ephys systems and re-sampled to 1000 Hz for computational purposes. The localization of electrodes was achieved through the co-registration of pre-operative MRI with a computer tomography (CT) scan, which was performed after the electrodes had been implanted. For each electrode, the location (x,y) and size (sigma) of the population receptive field (pRF) were taken from the previous calculation of the Hermes et al. (2019) second-order contrast (SOC) model, representing the location of the image to which the electrode responds.

Macaque Recordings

The animal (monkey H) was positioned 83 cm in front of a 22-inch 120Hz LCD monitor. Monkeys self-initiated trials by fixating on a small fixation spot presented at the center of the screen and had to maintain fixation during the entire trial. Trials were aborted during which the eye position deviated from the fixation spot by more than 0.8 visual deg radius. Correct trials were rewarded with diluted fruit juice. We analyzed only correctly performed trials. Recordings were made using a Tucker Davis Technologies (TDT) system. The data were filtered between 0.35 and 7500Hz (3 dB filter cutoffs) and digitized at 24.4 kHz (TDT PZ2 preamplifier). Line noise was removed using a two-pass 4th order Butterworth bandstop filters between 49.9-50.1, 99.7-100.3, and 149.5-150.5Hz. We downsampled the LFPs to ≈1.02kHz using Matlab's decimate.m function. For further details, see (Peter et al., 2019; Uran et al., 2022).

Stimuli and task

Human subjects were repeatedly presented with each type of stimulus image (15 trials per image) for a period of 500 ms at an approximate visual angle of 20° and viewing distance of 50 cm, with a baseline period between each presentation of the same duration, while maintaining fixation on a dot in the center of the screen. Stimuli consisted of 86 gray-scale patterns with gratings, curved lines, and noise patterns with 3 cycles per degree spatial frequencies. These patterns varied across well-controlled image dimensions, including special aperture, orientation, contrast, sparsity, and coherence (Hermes et al., 2019). Unlike the human subjects, Monkey-H was presented with natural stimuli for the original study and one oriented grating per session of the first four sessions recorded (20 trials per image). As such, to mirror our human analysis as closely as possible, we used LPIPS to quantify the mode least predictable natural stimuli over V1 channels and per session, thus selecting 80 trials per the two image categories. This allowed us to contrast the grating and natural stimuli to decode image homogeneity.

Image homogeneity analysis

For both human and macaque subjects we used an object-recognition convolutional neural network (OR-CNN) developed by Uran et al. (2022) to quantify the spatial predictability of each image for each channel (for homogeneous images the content of an area can be predicted by its spatial surroundings). In brief, this network models the visual system as an OR-CNN,

Images were first cropped from their original size of 880 x 880 px to 224 px around the center of each electrode's pRF.

To calculate predictability scores per electrode and type of image, we adapted the pred.py script from the model's Unet-Pred repository, maintaining the same weights and hyper-parameters. Each image was masked 26 pixels from its center in width and height and fed to the UNet model with one step per image. LPIPS predictability scores were then calculated between the model's predicted value for that central 104 x 104 pixels area and the true pixel values within the region for each image.

We then ranked the image categories by their predictability scores and used a two-sided t-test to compare the homogeneity of oriented gratings against noise and natural images.

Separating BB from NBG signals

Many methods that extract power in specific frequency bands are unable to discriminate between BB and narrowband oscillations (e.g., NBG). For example, extracting power in the gamma (30-70 Hz) using a bandpass filter will contain both narrow band oscillations and the portion of BB power within 30-70 Hz (Donoghue et al., 2020; Miller et al., 2009b). To isolate the BB and NBG components of our raw ECoG recordings, we performed spectral decoupling (Canales-Johnson et al., 2021; Miller et al., 2009a; Miller, 2019). In brief, the power spectral density (PSD) was computed during the presentation of all decoded images, normalized by the average power at each frequency, and log-transformed. Principle component analysis was applied to each PSD, which entails the eigendecomposition of the PSD's covariance matrix. These eigenvectors correspond to Spectral Principal Components (SPCA), representing distinct neural processing components (i.e., BB and NBG), enabling us to identify stimulus-related changes. Then, we reconstructed the BB and NBG of the individual trials by projecting the first and second SPCA, respectively, back into the ECoG voltage time series from -100 ms to 350 ms around the onset of each image. Afterward, the time series were z-scored per trial to get intuitive units, then exponentiated and subtracted by 1. For Monkey H, we down-sampled the reconstructed time series from 1000Hz to 500Hz. Finally, a baseline correction was performed by subtracting the mean value of the pre-stimulus period of -100 to 0 ms.

On visual inspection of the SPCA weights of the NBG signals, 3 electrodes (S1: V3 ventral; S2: V2 ventral, V2 ventral were found to have no characteristic component in the narrowband gamma range. Then, we only excluded these electrodes

from further MI and co-I analyses of the NBG signals. Hence, the number of electrodes analyzed for the within-electrode co-I analyses was 7 for BB and 4 for NBG signals in the case of S1 (Figure 3), and 6 for BB and 5 for NBG signals in the case of S2 (Figure 4). Consequently, the number of electrode pairs analyzed for the between-electrode co-I analyses were 12 for BB and 4 for NBG signal pairs for S1 (Figure 5), and 8 BB and 6 NBG signal pairs for S2 (Figure 6).

Mutual Information analyses

Mutual Information (MI) is the reduction in entropy of one variable when another variable is present. It quantifies the effect size of the conditional relationship between entropy across trials at a time-point and the given trial type, standardized in bits. Thus, the resultant MI reflects the amount of discriminant information present at the calculated time point between those trial categories. To quantify the MI between the categories of images and the BB and NBG signals, the GCMI toolbox (Gaussian Copula Mutual Information) (Ince et al., 2017) was used. The approach combined a permutation test with 200 permutations with a method of maximum statistics to correct for multiple comparisons. Using all available trials per category contrast, the signal at every time point was permuted 200 times for each electrode, randomly assigning the stimulus class labels each time. The maximum value at each time point was taken, and the 95th percentile of this value was used as the threshold for significance. This method corrects for multiple comparisons and provides a Family-Wise Error Rate (FWER) of 0.05. The electrodes listed in the previous section were used separately to compare orientation versus unfiltered noise and orientation versus filtered noise for the BB and NBG signals.

Co-information analyses

We quantified co-information (co-I) within signals (single electrodes) and between signals (between pairs of electrodes) using the GCMI toolbox (Ince et al., 2017). For the analyses based on the spectral decoupling method (Figures 3-6), the co-I was calculated on the BB and NBG signals separately, using the electrodes reported in the previous sections. The resulting co-I metric (in bits) quantifies the information content, redundant or synergistic, between the two signals. Co-I is formally expressed as:

$$\text{co-I}(X; Y; S) = I(X; S) + I(Y; S) - I(X, Y; S)$$

For each time point, $I(X; S)$ corresponds to the mutual information (MI) between the signal at recording site X and stimuli class S. $I(Y; S)$ corresponds to the MI between the signal at recording site Y and stimuli class S. Finally, $I(X, Y; S)$ corresponds to the MI between stimuli class S combining signals from recording sites X and Y.

Positive co-information shows that signals between recording sites contain redundant (or shared) information about the stimulus contrast. Negative co-information corresponds to the synergy between the two variables: the information when considering the two variables jointly is larger than when considering the variables separately. Figure 1A shows a schematic representation of co-I between two signals. It shows the independent information that signal 1 (S1) and signal 2 (S2) (both in white) contain. If there is an overlap in the information represented by the two signals, there is a redundancy (red color) in the information the two responses contain. If the two signals considered together contain more information than could be expected based on the information in the individual signals, there is synergy (blue color). Statistical analyses of co-I charts were performed using a permutation test with 200 permutations and the same maximum statistics method described for the MI analyses, resulting in an FWER of 0.05.

To statistically compare the BB and NBG signals, we performed two-tailed t-tests separately for co-I, redundancy, and synergy. For within-area contrasts (Figures 3 and 5), t-tests were performed on the normalized count (i.e., percentage) of significant time points (obtained from the previous step described above) per electrode. In the case of the between-area contrasts (Figures 4 and 6), t-tests were performed on the normalized count of significant time points between all pairs of electrodes for the corresponding BB and NBG signals.

Let $\text{coI}^*(t_{\text{ch}_a}, t_{\text{ch}_b}, \text{ch})$ represent the significant co-information, where t_{ch_a} and t_{ch_b} denote time indices, and ch denotes the channel index. The count of significant co-information over the first two dimensions (time × time) for each channel ch is given by:

$$\text{N co-I}^*(\text{ch}) = \sum_{t_{\text{ch}_a}, t_{\text{ch}_b}} \text{coI}^*(t_{\text{ch}_a}, t_{\text{ch}_b}, \text{ch}),$$

where t_{ch_a} and t_{ch_b} range over all time indices.

References

Akam, T.E., Kullmann, D.M., 2012. Efficient "Communication through Coherence" requires oscillations structured to minimize interference between signals. PLOS Comp. Biol. 8, e1002760. doi:10.1371/journal.pcbi.1002760.

Allen, W.E., Chen, M.Z., Pichamoorthy, N., Tien, R.H., Pachitariu, M., Luo, L., Deisseroth, K., 2019. Thirst regulates motivated behavior through modulation of brainwide neural population dynamics. Science 364, 253.

Blume, C., Dauphin, M., Niedernhuber, M., Spitschan, M., Meyer, M.P., Cajochen, C., Bekinschtein, T., Canales-Johnson, A., 2024. Reduced and redundant: Information processing of prediction errors during sleep.

Bressler, S.L., Kelso, J.S., 2001. Cortical coordination dynamics and cognition. Trends in cognitive sciences 5, 26–36.

Buzsáki, G., 2006. Rhythms of the Brain. Oxford University Press, USA.

Canales-Johnson, A., Beerendonk, L., Chennu, S., Davidson, M.J., Ince, R.A.A., van Gaal, S., 2023. Feedback information transfer in the human brain reflects bistable perception in the absence of report. PLOS Biology 21, e3002120. URL: http://dx.doi.org/10.1371/journal.pbio.3002120, doi:10.1371/journal.pbio.3002120.

Canales-Johnson, A., Billig, A.J., Olivares, F., Gonzalez, A., Garcia, M.d.C., Silva, W., Vaucheret, E., Ciraolo, C., Mikulan, E., Ibanez, A., Huepe, D., Noreika, V., Chennu, S., Bekinschtein, T.A., 2020. Dissociable Neural Information Dynamics of Perceptual Integration and Differentiation during Bistable Perception. Cerebral Cortex 30, 4563–4580. doi:10.1093/cercor/bhaa058.

Canales-Johnson, A., Teixeira Borges, A.F., Komatsu, M., Fujii, N., Fahrenfort, J.J., Miller, K.J., Noreika, V., 2021. Broadband dynamics rather than frequency-specific rhythms underlie prediction error in the primate auditory cortex 41, 9374–9391.

Chalk, M., Gutkin, B., Denève, S., 2016. Neural oscillations as a signature of efficient coding in the presence of synaptic delays. eLife 5. doi:10.7554/eLife.13824.

Chen, S., Liu, Y., Wang, Z.A., Colonell, J., Liu, L.D., Hou, H., Tien, N.W., Wang, T., Harris, T., Druckmann, S., Li, N., Svoboda, K., 2024. Brain-wide neural activity underlying memory-guided movement. Cell 187, 676–691.e16.

Cohen, U., Chung, S., Lee, D.D., Sompolinsky, H., 2020. Separability and geometry of object manifolds in deep neural networks. Nature communications 11, 1–13.

Combrisson, E., Basanisi, R., Gueguen, M.C., Rheims, S., Kahane, P., Bastin, J., Brovelli, A., 2024. Neural interactions in the human frontal cortex dissociate reward and punishment learning. Elife 12, RP92938.

Daube, C., Ince, R.A.A., Gross, J., 2019. Simple acoustic features can explain phoneme-based predictions of cortical responses to speech. Curr. Biol. 29, 1924–1937.e9.

Delis, I., Ince, R.A.A., Sajda, P., Wang, Q., 2022. Neural encoding of active multi-sensing enhances perceptual decision-making via a synergistic cross-modal interaction. J. Neurosci. 42, 2344–2355.

DiCarlo, J.J., Zoccolan, D., Rust, N.C., 2012. How does the brain solve visual object recognition? Neuron 73, 415–434.

Donoghue, T., Haller, M., Peterson, E.J., Varma, P., Sebastian, P., Gao, R., Noto, T., Lara, A.H., Wallis, J.D., Knight, R.T., et al., 2020. Parameterizing neural power spectra into periodic and aperiodic components. Nature neuroscience 23, 1655–1665.

Dowdall, J.R., Schneider, M., Vinck, M., 2023. Attentional modulation of inter-areal coherence explained by frequency shifts. Neuroimage 277, 120256.

Dowdall, J.R., Vinck, M., 2023. Coherence fails to reliably capture inter-areal interactions in bidirectional neural systems with transmission delays. Neuroimage 271, 119998.

Down, K.J., Mediano, P.A., 2025. Algebraic representations of entropy and fixed-sign information quantities. Entropy 27, 151.

Effenberger, F., Carvalho, P., Dubinin, I., Singer, W., 2025. The functional role of oscillatory dynamics in neocortical circuits: A computational perspective. Proc. Natl. Acad. Sci. U. S. A. 122, e2412830122.

Francis, N.A., Mukherjee, S., Koçillari, L., Panzeri, S., Babadi, B., Kanold, P.O., 2022. Sequential transmission of task-relevant information in cortical neuronal networks. Cell Rep. 39, 110878.

Freeman, W.J., Skarda, C.A., 1985. Spatial eeg patterns, non-linear dynamics and perception: the neo-sherringtonian view. Brain Research Reviews 10, 147–175.

Fries, P., 2005. A mechanism for cognitive dynamics: neuronal communication through neuronal coherence. Trends in Cognitive Sciences 9, 474–480. doi:10.1016/j.tics.2005.08.011.

Fries, P., Nikolić, D., Singer, W., 2007. The gamma cycle. Trends in Neurosciences 30, 309–316. doi:10.1016/j.tins.2007.05.005.

Gelens, F., Äijälä, J., Roberts, L., Komatsu, M., Uran, C., Jensen, M.A., Miller, K.J., Ince, R.A., Garagnani, M., Vinck, M., et al., 2024. Distributed representations of prediction error signals across the cortical hierarchy are synergistic. Nature Communications 15, 3941.

Greco, A., Moser, J., Preissl, H., Siegel, M., 2024. Predictive learning shapes the representational geometry of the human brain. Nat. Commun. 15, 9670.

Hermes, D., Miller, K., Wandell, B., Winawer, J., 2015a. Stimulus dependence of gamma oscillations in human visual cortex. Cereb. Cortex. 25, 2951–2959. doi:10.1093/cercor/bhu091.

Hermes, D., Miller, K.J., Wandell, B.A., Winawer, J., 2015b. Gamma oscillations in visual cortex: the stimulus matters. Trends Cogn. Sci. 19, 57–58.

Hermes, D., Nguyen, M., Winawer, J., 2017. Neuronal synchrony and the relation between the blood-oxygen-level dependent response and the local field potential. PLoS Biol. 15, e2001461.

Hermes, D., Petridou, N., Kay, K.N., Winawer, J., 2019. An image-computable model for the stimulus selectivity of gamma oscillations. Elife 8, e47035.

Ince, R.A., Giordano, B.L., Kayser, C., Rousselet, G.A., Gross, J., Schyns, P.G., 2017. A statistical framework for neuroimaging data analysis based on mutual information estimated via a gaussian copula. Human Brain Mapping 38, 1541–1573.

Ince, R.A.A., Jaworska, K., Gross, J., Panzeri, S., van Rijsbergen, N.J., Rousselet, G.A., Schyns, P.G., 2016. The deceptively simple N170 reflects network information processing mechanisms involving visual feature coding and transfer across hemispheres. Cereb. Cortex 26, 4123–4135.

Kar, K., Kubilius, J., Schmidt, K., Issa, E.B., DiCarlo, J.J., 2019. Evidence that recurrent circuits are critical to the ventral stream's execution of core object recognition behavior. Nature neuroscience 22, 974–983.

Khilkevich, A., Lohse, M., Low, R., Orsolic, I., Bozic, T., Windmill, P., Mrsic-Flogel, T.D., 2024. Brain-wide dynamics linking sensation to action during decision-making. Nature 634, 890–900.

King, J.R., Dehaene, S., 2014. Characterizing the dynamics of mental representations: the temporal generalization method. Trends Cogn. Sci. 18, 203–210.

Koçillari, L., Celotto, M., Francis, N.A., Mukherjee, S., Babadi, B., Kanold, P.O., Panzeri, S., 2023. Behavioural relevance of redundant and synergistic stimulus information between functionally connected neurons in mouse auditory cortex. Brain Inform. 10, 34.

Lewis, C.M., Ni, J., Wunderle, T., Jendritza, P., Lazar, A., Diester, I., Fries, P., 2021. Cortical gamma-band resonance preferentially transmits coherent input. Cell reports 35, 109083.

Luppi, A.I., Mediano, P.A.M., Rosas, F.E., Holland, N., Fryer, T.D., O'Brien, J.T., Rowe, J.B., Menon, D.K., Bor, D., Stamatakis, E.A., 2022. A synergistic core for human brain evolution and cognition. Nat. Neurosci. 25, 771–782.

Miller, K., Zanos, S., Fetz, E., Den Nijs, M., Ojemann, J., 2009a. Decoupling the cortical power spectrum reveals real-time representation of individual finger movements in humans. J. Neurosci. 29, 3132–3137.

Miller, K.J., 2019. A library of human electrocorticographic data and analyses. Nat. Hum. Behav. 3, 1225–1235.

Miller, K.J., Hermes, D., Pestilli, F., Wig, G.S., Ojemann, J.G., 2017. Face percept formation in human ventral temporal cortex. Journal of Neurophysiology 118, 2614–2627. URL: https://doi.org/10.1152/jn.00113.2017, doi:10.1152/jn.00113.2017.

Miller, K.J., Sorensen, L.B., Ojemann, J.G., Den Nijs, M., 2009b. Power-law scaling in the brain surface electric potential. PLoS computational biology 5, e1000609.

Nigam, S., Pojoga, S., Dragoi, V., 2019. Synergistic coding of visual information in columnar networks. Neuron 104, 402–411.e4.

Olivares, J., Orio, P., Sadilek, V., Schmachtenberg, O., Canales-Johnson, A., 2022. Odorant representations indicate nonlinear processing across the olfactory system.

Park, H., Ince, R.A.A., Schyns, P.G., Thut, G., Gross, J., 2018. Representational interactions during audiovisual speech entrainment: Redundancy in left posterior superior temporal gyrus and synergy in left motor cortex. PLOS Biology 16, 1–26.

Peter, A., Uran, C., Klon-Lipok, J., Roese, R., Van Stijn, S., Barnes, W., Dow-

dall, J.R., Singer, W., Fries, P., Vinck, M., 2019. Surface color and predictability determine contextual modulation of V1 firing and gamma oscillations. eLife 8, e42101.

Ray, S., Maunsell, J.H., 2015. Do gamma oscillations play a role in cerebral cortex? Trends in cognitive sciences 19, 78–85.

Ray, S., Maunsell, J.H.R., 2011. Different Origins of Gamma Rhythm and High-Gamma Activity in Macaque Visual Cortex. PLOS Biol. 9, e1000610. doi:10.1371/journal.pbio.1000610.

Sabra, Z., Bonilha, L., Naselaris, T., 2019. Spectral encoding of seen and attended object categories in the human brain. The Journal of Neuroscience 40, 327–342. URL: https://doi.org/10.1523/jneurosci.0900-19.2019, doi:10.1523/jneurosci.0900-19.2019.

Salinas, E., Sejnowski, T.J., 2001. Correlated neuronal activity and the flow of neural information. Nat Rev Neurosci 2, 539–50.

Sani, O.G., Pesaran, B., Shanechi, M.M., 2024. Dissociative and prioritized modeling of behaviorally relevant neural dynamics using recurrent neural networks. Nat. Neurosci. 27, 2033–2045.

Schneider, M., Broggini, A.C., Dann, B., Tzanou, A., Uran, C., Sheshadri, S., Scherberger, H., Vinck, M., 2021. A mechanism for inter-areal coherence through communication based on connectivity and oscillatory power. Neuron 109, 4050–4067.

Schneider, M., Tzanou, A., Uran, C., Vinck, M., 2023. Cell-type-specific propagation of visual flicker. bioRxiv .

de Schotten, M.T., Forkel, S.J., 2022. The emergent properties of the connected brain. Science 378, 505–510.

Shenoy, K.V., Kao, J.C., 2021. Measurement, manipulation and modeling of brain-wide neural population dynamics. Nat. Commun. 12, 633.

Shirhatti, V., Ravishankar, P., Ray, S., 2022. Gamma oscillations in primate primary visual cortex are severely attenuated by small stimulus discontinuities. PLoS biology 20, e3001666.

Singer, W., 1999. Neuronal synchrony: a versatile code for the definition of relations? Neuron 24, 49–65.

Spyropoulos, G., Saponati, M., Dowdall, J.R., Schölvinck, M.L., Bosman, C.A., Lima, B., Peter, A., Onorato, I., Klon-Lipok, J., Roese, R., et al., 2022a. Spontaneous variability in gamma dynamics described by a damped harmonic oscillator driven by noise. Nature communications 13, 1–18.

Spyropoulos, G., Schneider, M., van Kempen, J., Gieselmann, M.A., Thiele, A., Vinck, M., 2022b. Distinct feedforward and feedback pathways for cell-type specific attention effects. bioRxiv .

Steinmetz, N.A., Zatka-Haas, P., Carandini, M., Harris, K.D., 2019. Distributed coding of choice, action and engagement across the mouse brain. Nature 576, 266–273. doi:10.1038/s41586-019-1787-x.

Stringer, C., Pachitariu, M., Steinmetz, N., Reddy, C.B., Carandini, M., Harris, K.D., 2019. Spontaneous behaviors drive multidimensional, brainwide activity. Science 364, 255.

Terada, Y., Toyoizumi, T., 2024. Chaotic neural dynamics facilitate probabilistic computations through sampling. Proc. Natl. Acad. Sci. U. S. A. 121, e2312992121.

Timme, N., Alford, W., Flecker, B., Beggs, J.M., 2014. Synergy, redundancy, and multivariate information measures: an experimentalist's perspective. Journal of computational neuroscience 36, 119–140.

Tononi, G., Boly, M., Massimini, M., Koch, C., 2016. Integrated information theory: from consciousness to its physical substrate. Nature reviews neuroscience 17, 450–461.

Urai, A.E., Doiron, B., Leifer, A.M., Churchland, A.K., 2022. Large-scale neural recordings call for new insights to link brain and behavior. Nat. Neurosci. 25, 11–19.

Uran, C., Peter, A., Lazar, A., Barnes, W., Klon-Lipok, J., Shapcott, K.A., Roese, R., Fries, P., Singer, W., Vinck, M., 2022. Predictive coding of natural images by v1 firing rates and rhythmic synchronization. Neuron 110, 1240–1257.

Varela, F., Lachaux, J.P., Rodriguez, E., Martinerie, J., 2001. The brainweb: phase synchronization and large-scale integration. Nat. Rev. Neurosci. 2, 229–239.

Varley, T.F., Sporns, O., Schaffelhofer, S., Scherberger, H., Dann, B., 2023. Information-processing dynamics in neural networks of macaque cerebral cortex reflect cognitive state and behavior. Proc. Natl. Acad. Sci. U. S. A. 120, e2207677120.

Vinck, M., Bosman, C.A., 2016. More gamma more predictions: Gamma-synchronization as a key mechanism for efficient integration of classical receptive field inputs with surround predictions. Front Syst Neurosci 10, 35.

Vinck, M., Lima, B., Womelsdorf, T., Oostenveld, R., Singer, W., Neuenschwander, S., Fries, P., 2010. Gamma-Phase Shifting in Awake Monkey Visual Cortex. J. Neurosci. 30, 1250–1257. doi:10.1523/JNEUROSCI.1623-09.2010.

Vinck, M., Uran, C., Dowdall, J.R., Rummell, B., Canales-Johnson, A., 2025. Large-scale interactions in predictive processing: oscillatory versus transient dynamics. Trends Cogn. Sci. 29, 133–148.

Vinck, M., Uran, C., Spyropoulos, G., Onorato, I., Broggini, A.C., Schneider, M., Canales-Johnson, A., 2023. Principles of large-scale neural interactions. Neuron 111, 987–1002.

Vinck, M., Womelsdorf, T., Fries, P., 2013. Gamma-band synchronization and information transmission, in: Quiroga-Quian, R., Panzeri, S. (Eds.), Principles of Neural Coding. CRC Press.

Yang, Q., Walker, E., Cotton, R.J., Tolias, A.S., Pitkow, X., 2021. Revealing nonlinear neural decoding by analyzing choices. Nat. Commun. 12, 6557.